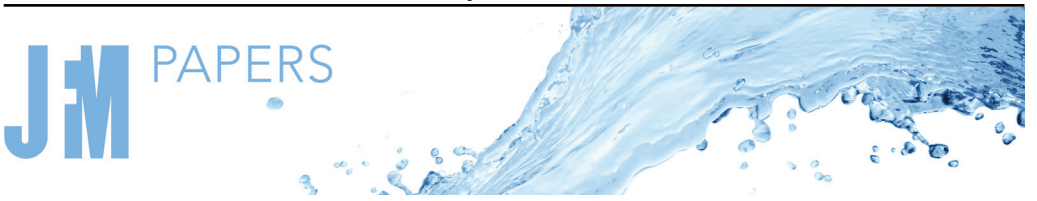
J. Fluid Mech. (2026), *vol.* 1026, A40, doi:10.1017/jfm.2025.11017



Scaling for compression waves/boundary layer interaction based on equivalent interaction intensity

Nan Li[1,2,3], **Xuanfei Yu**[4], **Zhengyin Ye**[1,2,3] and **Weiwei Zhang**[1,2,3]

[1]School of Aeronautics, Northwestern Polytechnical University, Xi'an 710072, PR China

[2]National Key Laboratory of Aircraft Configuration Design, Xi'an 710072, PR China

[3]International Joint Institute of Artificial Intelligence on Fluid Mechanics, Northwestern Polytechnical University, Xi'an 710072, PR China

[4]National Key Laboratory of Solid Rocket Propulsion, Northwestern Polytechnical University, Xi'an 710072, PR China

Corresponding author: Xuanfei Yu, yuxuanfei@nwpu.edu.cn

(Received 30 June 2025; revised 19 September 2025; accepted 28 November 2025)

The compression waves/boundary layer interaction (CWsBLI) in high-speed inlets poses significant challenges for predicting flow separation, rendering traditional shock wave/boundary layer interaction (SWBLI) scaling laws inadequate due to unaccounted effects of the coverage range of compression waves. This study aims to establish a unified scaling framework for CWsBLIs and SWBLIs by proposing an equivalent interaction intensity. Experiments were conducted in a Mach 2.5 supersonic wind tunnel, employing schlieren imaging and pressure measurements to characterise flows induced by curved surfaces at two deflection angles (10°, 12°) and varying coverage ranges of compression waves (d). An equivalent transformation method was developed to convert the CWsBLI into an equivalent incident SWBLI (ISWBLI), with interaction intensity derived from pressure gradients considering the coverage range. Key results reveal a critical threshold based on the interaction length of ISWBLI (L_{single}): when $d \leq L_{single}$, the interaction scale remains comparable to ISWBLI; when $d > L_{single}$, the weakened adverse pressure gradient leads to a reduction in the length scale. The proposed scaling framework unifies the CWsBLIs and SWBLIs, achieving better data collapse compared to the existing methods. This work advances our understanding of complex waves/boundary layer interactions, and provides a prediction method for the length scales of CWsBLIs.

Key words: boundary layer separation, supersonic flow, shock waves

© The Author(s), 2026. Published by Cambridge University Press.

https://doi.org/10.1017/jfm.2025.11017 Published online by Cambridge University Press

1. Introduction

Shock wave/boundary layer interaction (SWBLI) is a critical phenomenon in supersonic and hypersonic flows, profoundly affecting aircraft aerodynamic performance and structural reliability by inducing flow separation, high pulsating loads and localised heat transfer peaks. These effects pose particular challenges in the design of ramjet and scramjet engines, where the shock system configuration requires a careful trade-off between compression performance and flow stability for components such as inlets and isolators.

Extensive research has established scaling laws to predict the characteristic length scales of SWBLIs. The foundational work of Souverein, Bakker & Dupont (2013) successfully consolidated a wide range of experimental turbulent SWBLI data by attributing the interaction length to the mass flow deficit in the boundary layer. Subsequent studies refined this approach: Jaunet, Debieve & Dupont (2014) incorporated thermal wall effects, while Touré & Schülein (2020, 2023) and Xie *et al.* (2021) addressed limitations at high shock intensities by modifying the normalised interaction intensity. A correction methodology based on the theory of free interaction (Chapman, Kuehn & Larson 1957) has been widely applied in the interaction length scale under hypersonic conditions by researchers such as Helm & Martin (2021), Hong, Li & Yang (2021) and Zuo (2023). For transitional interactions, Mahalingesh, Piponniau & Dupont (2024) proposed a novel scaling that effectively collapses turbulent SWBLI data.

However, these established scaling laws face significant challenges when applied to internal flows within high-speed inlets. Unlike external flows, supersonic flows within inlets or isolators are constrained by geometry, leading to complex wave reflections (Wang, Xue & Tian 2017; Li *et al.* 2018; Zhang *et al.* 2021; Seckin *et al.* 2023). Multiple wave interactions markedly enhance the propensity for flow separation (Huang *et al.* 2015; Guan, Bai & Wu 2020; Li *et al.* 2021, 2024). Furthermore, to meet increasing performance demands, compression waves are increasingly utilised in place of discrete shocks to minimise pressure loss. Research concerning the interaction between compression waves and the boundary layer has received limited attention. In the compression waves/boundary layer interaction (CWsBLI), the role of baroclinicity in the formation of enhanced large-scale motions within the outer boundary layer and near-wall velocity patches has been noted by Wang *et al.* (2019). The resultant amplified vorticity further facilitates the interactive dynamics between the outer and inner fluid layers. Wen *et al.* (2023) also found that the adverse pressure gradient (APG) induced by compression waves can enhance the wake region of the boundary layer. However, in these studies, the boundary layer remains consistently in an attached state. Accurate prediction of the state of the CWsBLI is of critical importance for guiding the inlet design. Investigating the associated scaling laws not only possesses substantial engineering application value, but also enhances a deeper understanding of the interaction mechanisms between complex wave systems and the boundary layer.

Predicting the characteristic length scales of the CWsBLIs poses unique challenges. For SWBLIs, the primary determinant of the interaction length is the interaction intensity, which is related to the deflection angle of the flow (Settles, Bogdonoff & Vas 1976; Wang *et al.* 2015) or the pressure change of the flow passing through the interaction zone (Ramesh & Tannehill 2004; Souverein *et al.* 2013; Sriram & Jagadeesh 2015; Touré & Schülein 2020, 2023; Mahalingesh *et al.* 2024). While for CWsBLIs the ultimate pressure rise may be constant for a given flow deflection angle, the spatial coverage range of the compression waves significantly alters the length scale (Pang *et al.* 2025). This shows that traditional intensity metrics based solely on pressure rise or ratio are inadequate, as they

https://doi.org/10.1017/jfm.2025.11017 Published online by Cambridge University Press

M_1	U_1 (m s^{-1})	T_0 (K)	P_0 (kPa)	δ_1 (mm)	δ_1^* (mm)	θ_1 (mm)	Re_θ
2.33 ± 0.02	555.8 ± 5	295 ± 2	100 ± 0.5	7.49	1.96	0.53	5088

Table 1. Summary of flow conditions.

fail to capture the fundamental influence of the coverage range. Therefore, a new intensity characterisation that incorporates this geometric parameter is essential.

Therefore, the primary objective of this study is to investigate the scaling approach for CWsBLI. Schlieren imaging was used to analyse how the interaction length varies with the coverage range. An equivalent interaction intensity, derived from the pressure gradient imposed by compression waves, was subsequently proposed to characterise the features of CWsBLI. This parameter aims to establish a unified scaling law framework that is applicable to both SWBLI and CWsBLI. The paper is structured as follows. Section 2 outlines the experimental methodology and confirms the canonical nature of the incoming boundary layer. Section 3.1 presents the fundamental flow characteristics. Section 3.2 examines the interaction length, with particular focus on the applicability of the existing scaling law. Section 3.3 derives a new scaling law that applies to various coverage ranges of compression waves and integrates it with the established scaling law for turbulent SWBLI. Section 3.4 discusses the applicability and limitations of the newly proposed scaling law. Finally, the key findings of the study are summarised in § 4.

2. Experimental set-up

2.1. *Wind tunnel and test models*

Experiments were conducted in the Mach 2.50 supersonic wind tunnel of the National Key Laboratory of Aircraft Configuration Design at Northwestern Polytechnical University. A square nozzle with exit cross-section 200 mm $\times$ 200 mm was used. The operational run time of the facility is approximately 10 s. Two pieces of optical glass with dimensions 260 mm $\times$ 180 mm were mounted on each sidewall of the test section for schlieren imaging. The flow conditions used in this study are summarised in table 1. Here, T_0, and P_0 correspond to the stagnation temperature and the stagnation pressure of the supersonic flow at the exit of the nozzle, and U_1 denotes the edge velocity on the flat plate upstream of the interaction region. The Mach number upstream of the interaction region, denoted as M_1, is 2.33 ± 0.02, slightly lower than the freestream Mach number. This discrepancy can be attributed to the deceleration caused by a shock generated by the forced transition device positioned at the leading edge of the flat plate. The thickness of the boundary layer upstream of the interaction region was $\delta_1 = 7.49$ mm, the displacement thickness was $\delta_1^* = 1.96$ mm, the momentum thickness was $\theta_1 = 0.53$ mm, and the Reynolds number based on the momentum thickness was $Re_\theta = 5088$.

A full-span, 610 mm long steel plate with a forced transition device was used at the leading edge to generate the turbulent boundary layer for all tests. The plate was mounted 60 mm above the bottom wall of the test section via a rib plate. The rib plate was specifically designed to offset the divergence angle of the lower wall. Therefore, the full-span plate was parallel to the freestream flow. The incident shock and compression waves were generated using a wedge and a curved surface suspended from the upper wall, respectively. The aerodynamic profile of the curved surface was designed by tracking a streamline of the expansion waves passing over a sharp corner. Figure 1 shows the test model schematically. The flow deflection angles φ considered were 10° and 12°.

https://doi.org/10.1017/jfm.2025.11017 Published online by Cambridge University Press

Case	φ (deg.)	d (mm)	h (mm)	Case	φ (deg.)	d (mm)	h (mm)
A	10	0	85	I	12	0	90
B	10	15.2	85	J	12	26.8	90
C	10	32.1	85	K	12	49.6	90
D	10	46.3	80	L	12	64.9	90
E	10	58.1	80	M	12	72.0	90
F	10	59.4	85	N	12	75.1	80
G	10	69.8	85	O	12	78.2	80
H	10	84.7	85	P	12	80.9	90
				Q	12	96.9	90
				R	12	100.6	90

Table 2. Geometric parameters of test model.

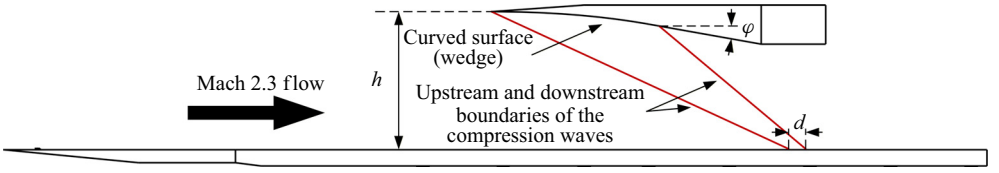


Figure 1. Schematic of the test model.

Each angle had different curved surface lengths to achieve varying coverage ranges (d) of compression waves, defined as the distance between the upstream and downstream boundaries of the compression waves under inviscid conditions. To ensure identical boundary layer conditions upstream of the interaction regions, the upstream boundaries of all compression waves originated from an approximately identical streamwise position. Table 2 presents the specific geometric parameters of different cases.

2.2. *Experimental measurement methods*

This study used pressure measurements and schlieren imaging to diagnose flow characteristics, as reported in Li *et al.* (2024). For the sake of completeness, we provide a brief introduction to these techniques below.

Thirty fast-response pressure transducers were positioned at 5.0 mm intervals in the streamwise direction, starting 390.0 mm from the leading edge, and spanning the interaction region. Two transducer models (Kulite XCS-062-15A and XCQ-062-30A) were used, with ranges 0–103.4 and 0–206.8 kPa, respectively. The transducers were connected to two A/D converters (NI PCI-6338 multifunction DAQ) and recorded simultaneously at 500 kS s^{-1} per channel. An auxiliary amplifier enhanced the pressure signal, but limited the response bandwidth to approximately 40 kHz. A low-pass filter with cut-off frequency 20 kHz was involved. The calibration of the fast-response transducers was performed by acquiring readings at 11 discrete pressure points ranging from 0.5 to 100 kPa, using a Wika Mensor pressure controller (CPC6000). A linear fitting method was used to establish a correlation between recorded pressure and mean voltage, with deviations within 0.5 %. Subsequently, a linear regression model was used to convert the voltage readings of the transducer into the corresponding pressure values.

A conventional Z-type schlieren system was used to visualise the flow structures. Two 200 mm diameter concave mirrors collimated and refocused light through the test section. A xenon lamp, positioned at the focal point of one mirror, directed light through a narrow

https://doi.org/10.1017/jfm.2025.11017 Published online by Cambridge University Press

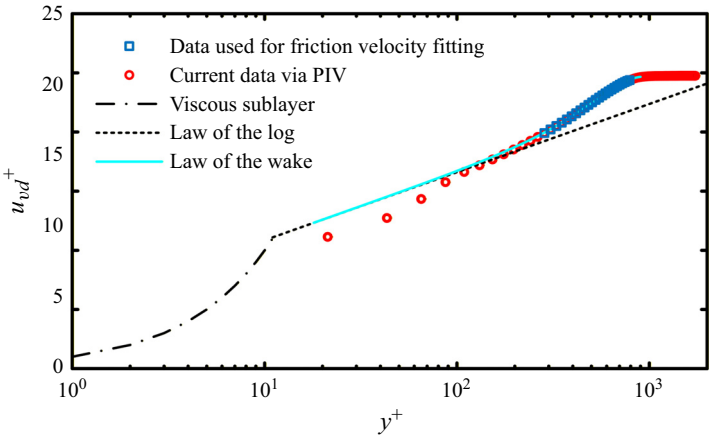


Figure 2. Velocity profile of the upstream turbulent boundary layer obtained by PIV.

slit. On the opposite side of the test section, another concave mirror collected the light rays, and a knife edge was placed horizontally at the focus to visualise the density gradients. Schlieren images were captured by a Phantom 340L high-speed camera at 1×10^4 fps with resolution 512×104 pixels and exposure time 2 µs.

2.3. *Incoming boundary layer profile*

The flow parameters of the undisturbed boundary layer were determined by utilising the particle image velocimetry (PIV) technique. Measurements were conducted 390 mm from the leading edge of the plate. The van Driest transformed mean velocity profile is presented in figure 2. The PIV data processing method has been presented in detail in Li *et al.* (2024). The statistical uncertainty associated with the mean velocity, due to limited realisations, is less than 1 % U_1. The transformed velocity profile matches well with the standard log law, and a distinct characteristic of the wake component of turbulent boundary layers can be clearly identified, which is in agreement with Coles' law of the wake (Coles 1956). The friction velocity $u_\tau = 25.77$ m s^{-1} was obtained by making a least squares fit to the law of the wake of the measured velocity profile. The corresponding skin friction coefficient C_f at the wall was 1.9×10^{-3}.

3. Results and discussion

3.1. *Basic flow features*

The schlieren images in figure 3 illustrate an exemplary case of the CWsBLI, with the key features of the flow structure schematically depicted in figure 3(c). The upstream and downstream boundaries of the compression waves were determined based on the variation in grey value resulting from changes in the density gradient, together with the inviscid solutions. The observed flow structure can be interpreted as follows. A separation bubble and a separated shear layer are induced by the APG, producing a separation shock. The compression waves interact with the separation shock and impinge on the separated shear layer, generating a series of expansion waves. Time-averaged schlieren images show that the expansion fans generated by the CWsBLI exhibit greater dispersion.

Prior to defining the interaction length of CWsBLI, we describe the interaction characteristics in terms of the separation scale. Figure 4 shows the flow structures resulting from CWsBLI in various configurations, in contrast to the incident SWBLI (ISWBLI).

https://doi.org/10.1017/jfm.2025.11017 Published online by Cambridge University Press

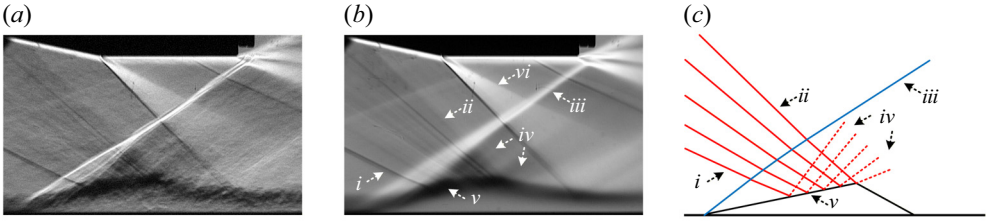


Figure 3. (*a*) An instantaneous schlieren image of the CWsBLI for $\varphi = 12°$ and $d = 27.8$ mm. (*b*) An average intensity map from 1.0×10^5 schlieren images for the same φ and d. (*c*) A schematic illustration (not to scale) of key flow features of the CWsBLI. Here, *i* is the upstream boundary of the compression waves, *ii* is the downstream boundary of the compression waves, *iii* is the separation shock induced by the CWsBLI, *iv* is expansion fans induced by the compression waves, *v* is the separated shear layer, and *vi* is expansion fans induced by the model.

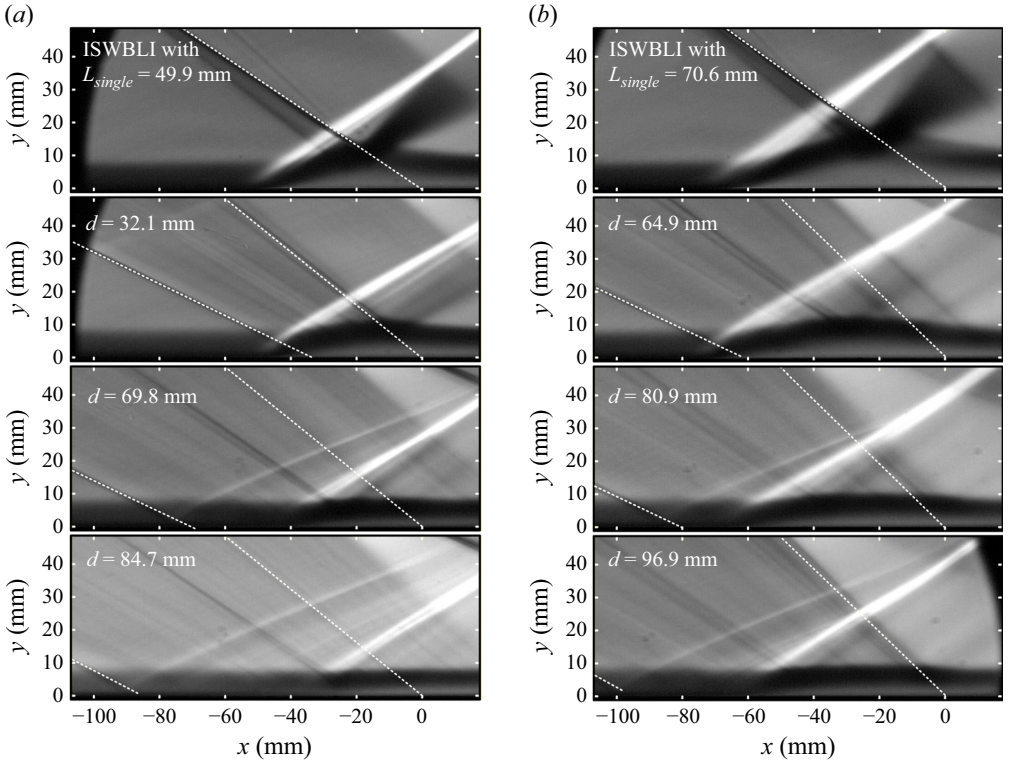


Figure 4. Time-averaged schlieren images of CWsBLIs compared to ISWBLIs at the same φ: (*a*) $\varphi = 10°$, (*b*) $\varphi = 12°$. The white dotted line represents either the incident shock or the boundaries of the compression waves. The origin is defined as the intersection point between the incident shock or the downstream boundary of the compression waves and the wall, and L_{single} denotes the interaction length of the ISWBLI.

All schlieren images are aligned in the flow direction according to the downstream boundary of the compression waves. By varying φ, comparing the characteristics of CWsBLI reveals that when d is relatively small, the induced flow separation aligns closely with that of ISWBLI. As d increases, the separation scale decreases progressively.

The pressure distributions within the interaction region are shown in figure 5. In this figure, the mean location of the shock foot, which was identified according to the peak of the pressure spectrum, was set as the origin. Sensor positions were normalised by L_{single}.

https://doi.org/10.1017/jfm.2025.11017 Published online by Cambridge University Press

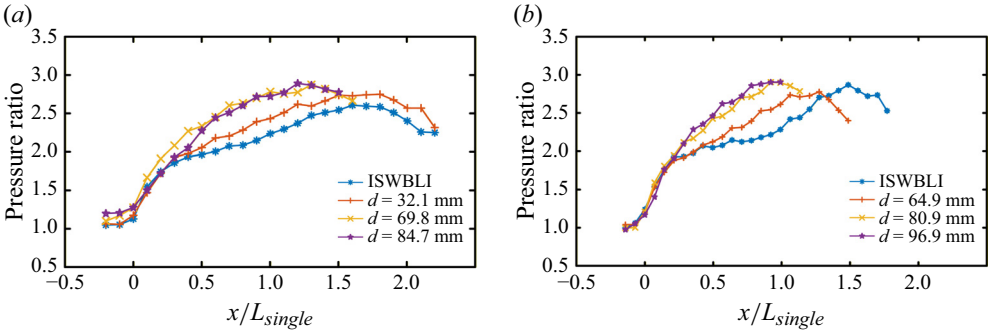


Figure 5. Pressure distributions along the bottom-wall centreline: (*a*) for $\varphi = 10°$, $p_{3,inv}/p_1 = 3.18$ in ISWBLI, and $p_{3,inv}/p_1 = 3.17$ in CWsBLI, respectively; (*b*) for $\varphi = 12°$, $p_{3,inv}/p_1 = 3.90$ in ISWBLI, and $p_{3,inv}/p_1 = 3.88$ in CWsBLI, respectively.

For ISWBLIs with different φ, the typical two-step pressure rise can be observed: an initial separation-induced pressure rise followed by a reattachment-induced pressure rise. In CWsBLI cases, the initial pressure rise exhibits a trend similar to that of a typical SWBLI, marked by a sharp pressure increase. In the subsequent region, instead of a pressure plateau, the pressure continues to increase due to the persistent influence of compression waves when $d \leq L_{single}$. The slope of this pressure rise closely corresponds to the second pressure rise in a typical SWBLI. When $d > L_{single}$, the pressure distribution becomes comparable to that of an attached SWBLI. It is important to note that as a result of the influence of expansion waves downstream of the model, the maximum pressure ratios are significantly lower than the theoretical inviscid values ($p_{3,inv}/p_1$). Furthermore, the larger the value of φ, the more pronounced this deviation becomes. The primary reason is that to minimise blockage, models with large φ are designed with a relatively compact configuration, thus reducing the distance between the expansion fan and the interaction region. Consequently, the effect of the pressure drop becomes more substantial.

Schlieren images show that the separation shock appears wider after time-averaged processing due to shock foot dispersion into multiple compression waves and the spanwise integration effect of the schlieren system. Therefore, maximum luminance points within the separation shock region were extracted at various heights without being affected by the expansion fan induced by the model. A straight line obtained through linear fitting served as an approximation of the separation shock. Figure 6(*a*) illustrates the variation in angles of the separation shock that correspond to different d relative to the ISWBLI with $d = 0$ mm. The angle of the separation shock in the ISWBLI reaches a maximum value. For CWsBLIs, the shock angle decreases as d increases until it approaches L_{single}. When $d > L_{single}$, the angle gradually increases again. The uncertainty associated with the separation shock angle is estimated to be approximately 0.5 %. While this level of uncertainty is comparable to the difference in shock angles observed between the cases $d = 72.0$ mm and $d = 75.1$ mm, where the interaction lengths are both close to L_{single}, the flow behaviour in the immediate vicinity of this critical point remains indeterminate. Nevertheless, the trends derived from data sufficiently distant from the critical point are considered reliable.

Schlieren images also show that the development of the separated shear layer varies with d. The minimum luminance points in the shear layer were identified, and a quadratic curve fitting method determined the trend line of shear layer development (see figure 6*b*). In this figure, the starting point of the shear layer is defined as the origin, and all positions are normalised with respect to L_{single}. For the ISWBLI with $d = 0$ mm, the shear layer

https://doi.org/10.1017/jfm.2025.11017 Published online by Cambridge University Press

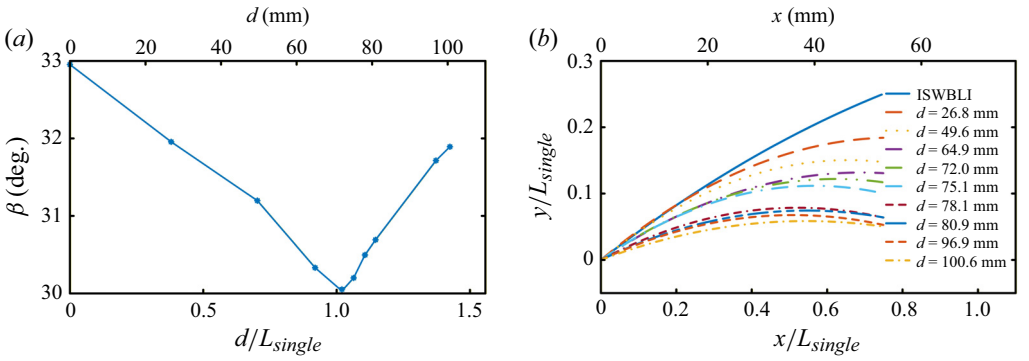


Figure 6. (*a*) Angles of the separation shocks and (*b*) development of the separated shear layers for CWsBLIs with $\varphi = 12°$ and varying d, compared to those of the ISWBLI.

angle reaches its maximum value, indicating the largest flow deflection and shock angles. For CWsBLIs, the downward-deflected flow induced by compression waves affects the shear layer. Broader coverage range reduces both the shear layer angle and the shock angle. When d approaches L_{single}, the shear layer developments for $d = 64.9$, 72.0 and 75.1 mm become similar, leading to nearly identical separation shock angles. When d exceeds L_{single}, variations in the shear layer angle become negligible, while the angle of the separation shock increases due to changes in the upstream Mach number caused by partial compression waves.

Figure 7(*a*) presents maps of the frequency-premultiplied power spectral density ($fG(f)$) of the pressure fluctuations with $\varphi = 12°$. The spectra are normalised by the variance of the local wall pressure below 20.0 kHz. In all scenarios, the peak energy should be located at the convection frequency $U_1/\delta_1 = 89.51$ kHz; however, these peaks fall near 20 kHz, which is caused by the filtering of the acquisition system. The presence of a weak low-frequency component below 500 Hz can be observed at the shock foot. Subsequently, high-frequency fluctuations emerge, indicating the incipient instability of the separated shear layer. For ISWBLI and CWsBLI with a relatively large separation scale, the subsequent shedding of the shear layer is found to shift towards lower frequencies as it develops along the recirculation region.

Figure 7(*b*) presents the streamwise evolution of the characteristic frequency f_{ch} under varying values of d. This f_{ch} is determined directly from the spectral peaks recorded at each sensor location, with estimated uncertainty approximately 5 %. Across all cases, f_{ch} exhibits a rapid increase in the low frequencies observed at the separation shock foot. It attains a local maximum at the inception of the shear layer, and subsequently decreases monotonically throughout the recirculation region until vortex shedding is initiated. As d increases, the characteristic frequency at the vortex shedding location gradually rises, and this process can be categorised into two different types. For $d \leq L_{single}$, the separation scale remains relatively unchanged, which means that the shear layer length does not vary significantly. However, with the expanding influence of compression waves, the upstream boundary gradually moves closer to the inception of the shear layer development. Consequently, the vortex structures forming within the shear layer are disrupted by compression waves and break up prematurely. As a result, these vortices do not develop as fully as they do in the case of SWBLI or when d is small, which ultimately leads to an increase in dominant frequency. When $d > L_{single}$, as described in figure 4, the reduction in the separation scale results in a shorter shear layer and smaller vortex structures, which in turn causes an increase in the characteristic frequency at the vortex shedding location.

https://doi.org/10.1017/jfm.2025.11017 Published online by Cambridge University Press

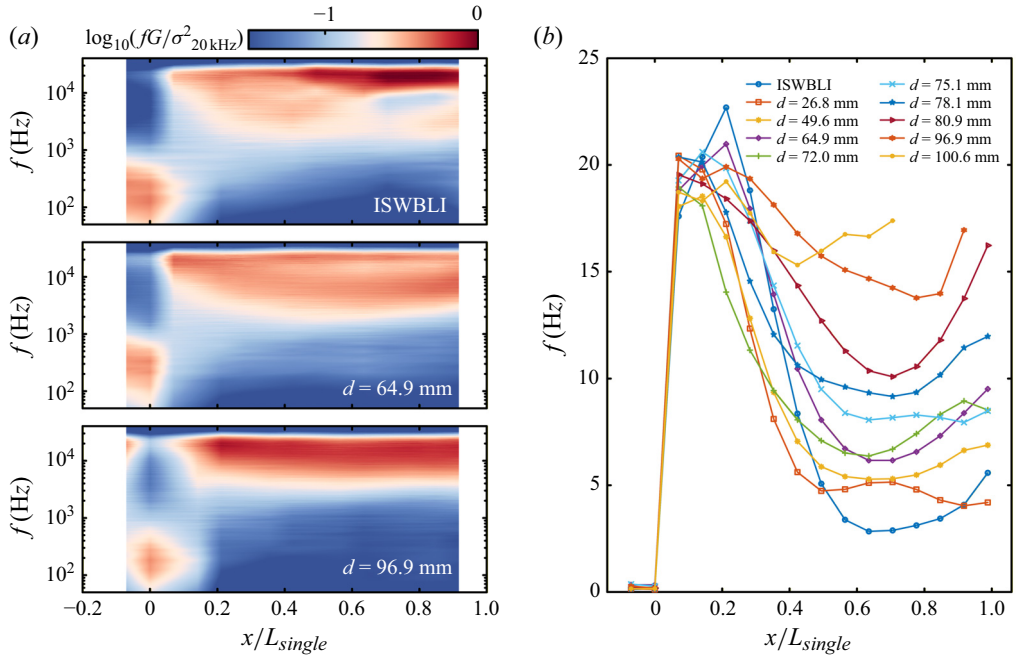


Figure 7. (*a*) Contours of the frequency-premultiplied pressure fluctuation power spectral density within the interaction region and (*b*) distributions of the dominant frequency f_{ch} in the shear layer evolution of the CWsBLI with $\varphi = 12°$ and increasing d, in comparison to the ISWBLI.

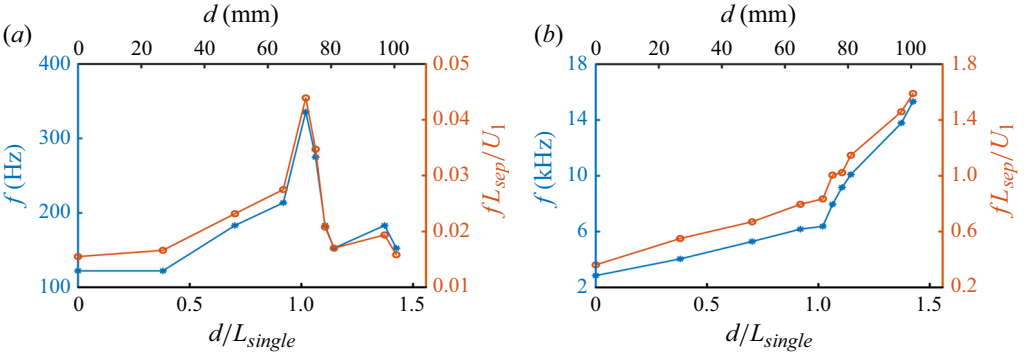


Figure 8. (*a*) Evolution of the dominant frequency of low-frequency oscillations at the separation shock foot, and (*b*) evolution of the dominant frequency of shear layer unsteadiness for the CWsBLI with $\varphi = 12°$ and increasing d, in comparison to the ISWBLI.

This trend is contrary to what has been previously observed in studies in which the separation scale increased (Li *et al.* 2024).

Figure 8(*a*) depicts the evolution of the low-frequency components associated with the separation shock oscillation and the characteristic frequency during the development of the shear layer with respect to d. The Strouhal numbers ($St_{L_{sep}} = fL_{sep}/U_1$) corresponding to these frequencies, computed based on their respective separation scales, fall within the low-frequency range. However, $St_{L_{sep}}$ associated with the shear layer transitions from medium to high frequency, indicating a decrease in flow separation and a transition towards turbulence-dominated behaviour. It is evident that the characteristic frequency changes as

https://doi.org/10.1017/jfm.2025.11017 Published online by Cambridge University Press

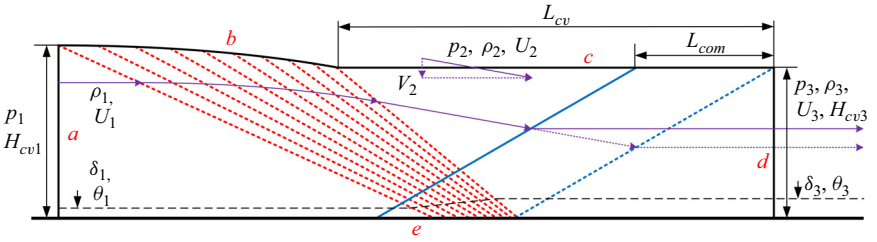


Figure 9. Control volume for the CWsBLI.

d approaches L_{single}. When $d \leq L_{single}$, the frequency of the low-frequency oscillation gradually increases. One possible explanation is that under conditions of larger-scale separation, internal mechanisms contribute to the instability, while compression waves interact with the shear layer, thereby influencing the shedding rate. This can be observed in the continuously increasing shedding frequency shown in figures 7(*b*) and 8(*b*). As d increases, the impact of compression waves on the shear layer becomes more significant. When $d > L_{single}$, the separation scale decreases, and the rate of the entrainment-recharge process accelerates. However, the dominant frequency of the low-frequency oscillation drops rapidly. The possible reason for this is that the decrease in the separation scale leads to a change in the dominant mechanism of the unsteadiness, from 'downstream mechanism' to 'upstream mechanism'. For example, low-frequency disturbances caused by the thin and pointed leading edge of the curved surface can be the main cause of the low-frequency oscillation of the separation shock. Figure 8(*b*) summarises the evolution of the characteristic frequency within the shear layer with respect to d. When the separation scale is relatively large (d is small), the characteristic frequency remains in the medium to high frequency range, with $St_{L_{sep}} = 0.2-1.0$. When the separation scale is small, the characteristic frequency shifts to the high-frequency band, showing turbulent characteristics.

3.2. *Length of interaction*

A clear and reasonable definition of the interaction length is essential for developing the scaling law. The interaction length, as a critical parameter, quantifies the extent of the disturbed boundary layer and can estimate the separation scale under specific conditions. For ISWBLIs, it refers to the distance between the mean location of the separation shock (or reflected shock) and the extrapolated wall impact point of the incident shock; for compression corners, it denotes the distance to the corner. This study defines the interaction length of CWsBLI (L_{com}) as the distance between the mean location of the separation shock (or reflected shock) and the extrapolated wall impact point of the downstream boundary of the compression waves, as illustrated in figure 9.

The flow model depicting the interaction between the compression waves and the turbulent boundary layer is presented in figure 9. Under the inviscid assumption, the compression waves reflected by the wall can be equivalently replaced by an oblique shock wave (indicated by the dotted blue line). When viscous effects are considered, the boundary layer is subjected to an APG due to compression waves. As a result, the reflected shock is translated upstream by L_{com} to ensure mass and momentum conservation. This length is defined as the interaction length. Based on this, a control volume enclosed by five surfaces (labelled a to e) is defined, and mass conservation equations are derived for both inviscid and viscous cases:

https://doi.org/10.1017/jfm.2025.11017 Published online by Cambridge University Press

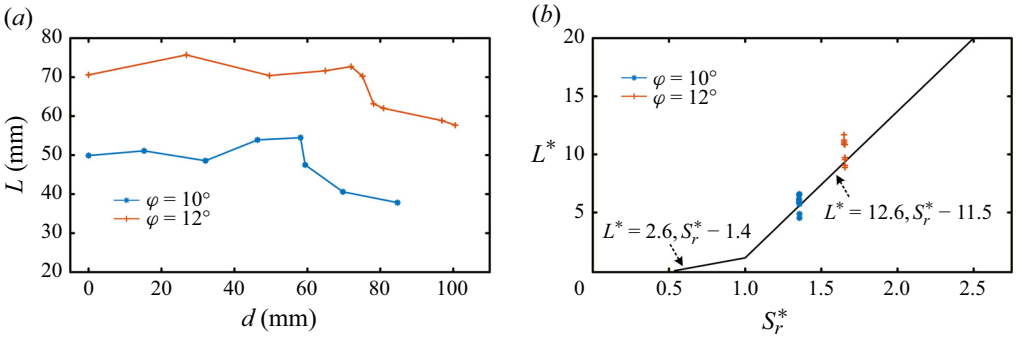


Figure 10. (*a*) Variation of the interaction length with different φ and d, and (*b*) scaling for CWsBLI based on the method proposed by Mahalingesh *et al.* (2024).

$$\rho_1 U_1 H_{cv1} + \rho_2 V_2 L_{cv} - \rho_3 U_3 H_{cv3} = 0, \tag{3.1}$$

$$\rho_1 U_1 \left(H_{cv1} - \delta_1^*\right) + \rho_2 V_2 (L_{cv} - L_{com}) - \rho_3 U_3 \left(H_{cv3} - \delta_3^*\right) = 0. \tag{3.2}$$

By substituting (3.2) into (3.1), the interaction length can be derived as

$$L_{com} = \frac{\rho_3 U_3 \delta_3^* - \rho_1 U_1 \delta_1^*}{\rho_2 V_2} = \frac{\rho_3 U_3 \delta_3^* - \rho_1 U_1 \delta_1^*}{\rho_2 U_2 \sin(\varphi)}. \tag{3.3}$$

The dimensionless characterisation of the interaction length was obtained by utilising the geometric shape factor G_3 and the boundary layer displacement thickness δ_1^*:

$$L_{com}^* = \frac{L_{com}}{\delta_1^*} G_3 = \frac{\rho_3 U_3 \delta_3^*}{\rho_1 U_1 \delta_1^*} - 1 = \frac{\dot{m}_{out}^*}{\dot{m}_{in}^*} - 1, \tag{3.4}$$

where

$$G_3 = \sin(\varphi) \frac{\rho_2 U_2}{\rho_1 U_1} = \sin(\varphi) \frac{M_2}{M_1} \left(\frac{1 + 0.5(\gamma - 1) M_1^2}{1 + 0.5(\gamma - 1) M_2^2} \right)^{\frac{\gamma+1}{2(\gamma-1)}}, \tag{3.5}$$

and the right-hand side of (3.4) will be replaced by the interaction intensity. The scaling of the interaction length for both CWsBLI and SWBLI is identical. The only distinction lies in the methodology used to determine G_3: in CWsBLI, G_3 is calculated based on the Prandtl–Meyer function and isentropic relations, while in SWBLI, G_3 is established using the oblique shock wave relation. Equation (3.4) relates the interaction length to geometric parameters, incoming flow conditions, and interaction intensity. Among these factors, the interaction intensity serves as a critical determinant of the length scale for both SWBLI and CWsBLI, traditionally quantified by the pressure rise (S_e^* proposed by Souverein *et al.* 2013) or the pressure ratio (S_r^* proposed by Mahalingesh *et al.* 2024).

Based on the definition of the interaction length for CWsBLIs and the scaling law proposed by Mahalingesh *et al.* (2024), figure 10 presents the variations of L_{com} under different φ and d, together with the corresponding scaling for L_{com}. It can be seen that when d is smaller than L_{single}, the interaction length essentially remains consistent with L_{single}. Possible reasons for the deviations may include the influence of the downstream expansion fan of the model on the interaction, which decreases the pressure rise during reattachment. This inference aligns well with the conclusion drawn by Fan *et al.* (2023). It is crucial to note that in scenarios where φ remains constant and the coverage range d exceeds L_{single}, the pressure rise across the interaction region remains largely unaffected

https://doi.org/10.1017/jfm.2025.11017 Published online by Cambridge University Press

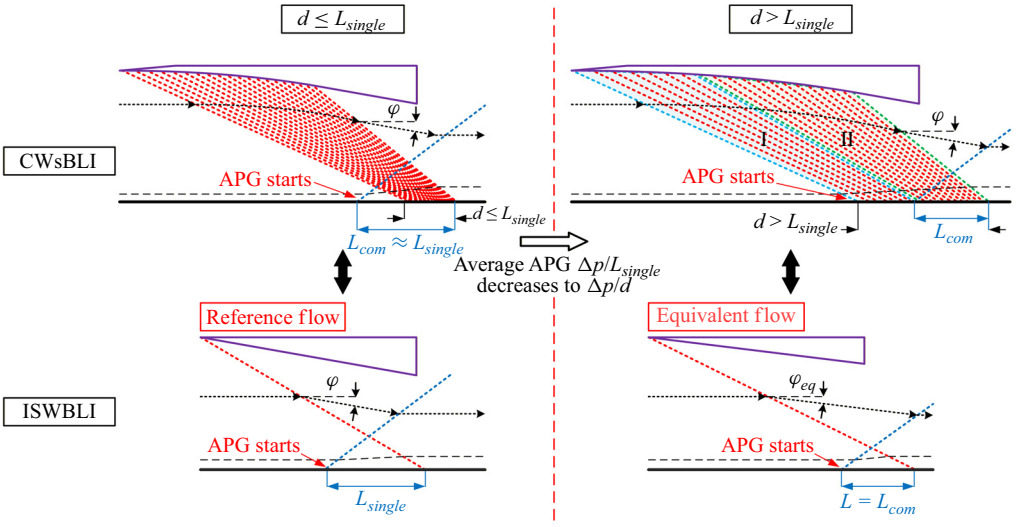


Figure 11. Classification of the CWsBLI and its equivalent ISWBLI case.

by further increases in d, irrespective of whether the results are obtained from inviscid solutions or experimental measurements. This variety in trends was greater than the uncertainty associated with the measurement techniques. This poses significant challenges in establishing the separation criterion for CWsBLIs, since an identical pressure rise or pressure ratio corresponds to the same interaction state. As shown in figure 10(*b*), based on the pressure ratio method, the scaling did not collapse the dataset of the CWsBLIs. Such data points fell on a straight vertical line under the same φ, with shorter lengths for longer coverage ranges. A likely reason is that the interaction intensity scaling does not account for the effect of the coverage range of the compression waves. Hence this study highlights the need to consider changes in the coverage range of compression waves when evaluating the interaction intensity.

3.3. *Scaling analysis based on equivalent interaction intensity*

The underlying reason for this misjudgement lies in the fact that the primary factor influencing the separation of the boundary layer is the pressure gradient. Our subsequent development of the scaling law starts from this consideration. Rather, if we were to adopt current methods, the influence of spatial scale would inevitably be mitigated. According to the aforementioned observations, under the same φ, the interaction length of the corresponding ISWBLI serves as a critical demarcation point. When d is either greater than or less than this value, the resulting length scales of the CWsBLI differ. Based on this characteristic, this study categorises CWsBLI into two types: type I, where $d \le L_{single}$, and type II, where $d > L_{single}$, as illustrated in figure 11. The ISWBLI induced by an incident shock with flow deflection angle φ is taken as the reference flow. An equivalent transformation approach is employed to convert CWsBLIs with varying coverage ranges into ISWBLIs exhibiting uniform interaction intensity. The key hypothesis is that two interactions producing the same interaction length must be driven by the same average APG, resulting in the same pressure rise in the interaction region. In CWsBLIs, the flow passing through the compression waves is assumed to be an isentropic process. Based on this classification and the associated hypotheses, subsequent discussions will focus on the scaling of these two types.

https://doi.org/10.1017/jfm.2025.11017 Published online by Cambridge University Press

3.3.1. *Type I: $d \leq L_{single}$*

For type I ($d \leq L_{single}$), the CWsBLI induced separation zone covers the region where compression waves impinge. Theoretical analysis shows that under the same φ, the inviscid pressure rise $\Delta p_{single,inv} = p_{3,single,inv} - p_1$ from ISWBLI is nearly equal to $\Delta p_{com,inv} = p_{3,com,inv} - p_1$ from CWsBLI at lower Mach numbers (as shown in the caption of figure 5). Here, $p_{3,com,inv}$ denotes the inviscid pressure downstream of the separation shock, with the flow through the compression waves assumed to be isentropic. This equivalence has also been experimentally validated at a lower Mach number. By analysing the experimental results, it is evident that CWsBLI under this condition exhibits an interaction length comparable to that of the reference flow. This observation can also be substantiated through proof by contradiction. Supposing that $L_{com} \neq L_{single}$, there are two possible scenarios: either $L_{com} < L_{single}$ or $L_{com} > L_{single}$.

Under the condition $L_{com} < L_{single}$, the pressure rise associated with CWsBLI occurs over a spatial scale of L_{com}. Assuming that the magnitudes of the pressure rises are equal (i.e. $\Delta p_{com,inv} = \Delta p_{single,inv}$), the resulting average pressure gradient caused by the CWsBLI, $\Delta p_{com,inv}/L_{com}$, is greater than that of the ISWBLI, $\Delta p_{single,inv}/L_{single}$. This suggests that the intensity of the compression waves, which is positively correlated with the pressure gradient, should be no less than that of the incident shock under the same φ. A stronger interaction typically corresponds to an extended interaction length; consequently, $L_{com} > L_{single}$. This conclusion contradicts the initial assumption that $L_{com} < L_{single}$.

If $L_{com} > L_{single}$, then $\Delta p_{com,inv}/L_{com} < \Delta p_{single,inv}/L_{single}$ (given $\Delta p_{com,inv} = \Delta p_{single,inv}$), which indicates that the intensity of the compression waves is weaker than that of the incident shock and thus results in a shorter interaction length. However, this contradicts the assumption that $L_{com} > L_{single}$. The only self-consistent condition is $L_{com} = L_{single}$, which ensures $p_{com,inv}/L_{com} = p_{single,inv}/L_{single}$. Therefore, for $d < L_{single}$, the length of the CWsBLI is comparable to that of the ISWBLI under the same φ. This conclusion is consistent with findings reported in the existing literature (Pang *et al.* 2025), and is consistent with current experimental results, with minor discrepancies likely attributable to the expansion fan produced by the model.

Given identical upstream boundary layer conditions, the pressure rises experienced by airflow passing through the two interaction regions (CWsBLI and SWBLI) are nearly equivalent, and the corresponding interaction lengths are also comparable. Therefore, when $d \leq L_{single}$, it is entirely reasonable to model the system using an ISWBLI with the same φ, and subsequently conduct a scaling analysis based on the SWBLI methodology.

3.3.2. *Type II: $d > L_{single}$*

For type II ($d > L_{single}$), the pressure rise within the interaction region originates from the upstream boundary of the compression waves, which distinguishes it from the previous type. In this context, the CWsBLI is substituted with an equivalent ISWBLI. The equivalent ISWBLI has the same Reynolds number, upstream Mach number, interaction length and interaction intensity as the original CWsBLI. Subsequently, the scaling can be performed in accordance with the methods proposed by Souverein *et al.* (2013) or Mahalingesh *et al.* (2024). During this process, two key considerations must be taken into account.

First, it is the pressure gradient rather than the pressure rise that primarily governs the flow separation and the mass-flow deficit ratio across the interaction. Assuming that the pressure rise induced by the wave system remains constant, the increase in the coverage range d directly contributes to a reduction in the average pressure gradient, which in turn reduces the size of the separation zone. Consequently, the average pressure gradient induced by compression waves, $\Delta p_{com,inv}/d$, which is also assumed to be equivalent to

https://doi.org/10.1017/jfm.2025.11017 Published online by Cambridge University Press

that in the separation region (region II in figure 11), serves as a critical parameter for the equivalent conversion. Therefore, the ISWBLI to be considered equivalent has the same pressure gradient as the CWsBLI:

$$\frac{\Delta p_{com,inv}}{\Delta x} = \frac{\Delta p_{equ,inv}}{\Delta x}. \tag{3.6}$$

Under condition $d > L_{single}$, the pressure gradient imposed on the boundary layer by the compression waves is given by $(p_{3,com,inv} - p_1)/d$. Consider an equivalent ISWBLI scenario with the same pressure gradient and interaction length L_{com}. The pressure rise for the equivalent ISWBLI is

$$\Delta p_{equ,inv} = (p_{3,com,inv} - p_1)\frac{L_{com}}{d}. \tag{3.7}$$

This study uses the pressure ratio method proposed by Mahalingesh *et al.* (2024) to characterise the intensity of CWsBLI. The equivalent pressure rise can be converted into the equivalent pressure ratio as

$$\left(\frac{p_{3,inv}}{p_1}\right)_{equ} = \frac{\Delta p_{equ,inv} + p_1}{p_1} = \left(\frac{p_{3,com,inv}}{p_1} - 1\right)\frac{L_{com}}{d} + 1. \tag{3.8}$$

Second, it is essential to ensure that two equivalent interactions exhibit identical interaction lengths. Given the Mach number M_1 and the interaction intensity determined previously, the flow deflection angle φ_{equ} of the equivalent ISWBLI can be established, which is crucial for determining G_3 in subsequent calculations. This consideration highlights an important issue. According to existing scaling laws for SWBLI, the interaction length can be determined solely based on M_1 and φ_{equ}. However, for CWsBLIs, this theoretically computed interaction length often deviates from the experimentally observed value L_{com}. To address this discrepancy, a correction is necessary to the initial separation pressure p_{sep} of the boundary layer, grounded in physical evidence.

The CWsBLI can be decomposed into an infinite series of discrete interactions that occur between each individual compression wave and the boundary layer. Within the interaction region, the pressure progressively increases in the streamwise direction, while the boundary layer's ability to resist flow separation gradually decreases. This decline in separation resistance is attributed to the cumulative impact of disturbances generated by each wave interaction. When the pressure rise and the corresponding reduction in the boundary layer's resistance exceed a critical threshold, flow separation is triggered. As shown in figure 11, the CWsBLI can be divided into two discrete parts: one partially covered by compression waves without flow separation (region I) and the other corresponding to the separated region (region II), which is covered by the remaining compression waves. The compression waves in region I initially interact with the boundary layer. Although this interaction does not lead to separation, the velocity deficits introduced into the boundary layer can influence the subsequent interaction. In region II, the compression waves interact with a perturbed boundary layer that differs from the corresponding boundary layer in the equivalent ISWBLI. Consequently, the interaction intensity p_{sep} responsible for the initial separation of the boundary layer must also be adjusted. Here, L_{com}/d also serves as a correction factor to determine this pressure ratio:

$$\left(\frac{p_{sep}}{p_1}\right)_{equ} = 1 + \frac{\gamma M_1^2}{2k}\left(\frac{L_{com}}{d}\right)^m. \tag{3.9}$$

https://doi.org/10.1017/jfm.2025.11017 Published online by Cambridge University Press

Considering the scenario of type I ($d \le L_{single}$), CWsBLIs with various d can be equivalent to ISWBLI with the same flow deflection angle. The influence of d can be deemed negligible. Therefore, introducing the correction factor L_{com}/d is unnecessary. To account for this behaviour, a piecewise function ξ is defined as follows: $\xi = 1$ when $d \le L_{single}$, and $\xi = L_{com}/d$ when $d > L_{single}$. By dividing (3.8) by (3.9), the dimensionless intensity of CWsBLI, denoted as S^*_{com}, is obtained as

$$S^*_{com} = \frac{(p_{3,com,inv}/p_1 - 1)\xi + 1}{1 + (\gamma M_1^2/2k)\xi^m}, \quad k = \begin{cases} 3.0, & \text{if } Re_\theta \le 1 \times 10^4, \\ 2.5, & \text{if } Re_\theta > 1 \times 10^4, \end{cases}$$
$$\xi = \begin{cases} 1, & \text{if } d \le L_{single}, \\ L_{com}/d, & \text{if } d > L_{single}. \end{cases} \tag{3.10}$$

In addition to characterising the interaction intensity, scaling the interaction length is another essential step. In the work by Souverein *et al.* (2013), a simplified model for the SWBLI was developed, leading to the derivation of the correction factor G_3, which quantifies the effects of geometric parameters and the Mach number of the incoming flow. For the equivalent ISWBLI, the flow deflection angle φ_{equ} can be determined based on the equivalent pressure ratio $(p_{3,inv}/p_1)_{equ}$ using the oblique shock relations, given a specified incoming Mach number M_1:

$$\left(\frac{p_{3,inv}}{p_1}\right)_{equ} = f(M_1, \varphi_{equ}) \Rightarrow \varphi_{equ}. \tag{3.11}$$

The geometric correction factor G_3 for the equivalent ISWBLI is given by $G_3 = \sin(\varphi_{equ})\sin(\beta)/\sin(\beta - \varphi_{equ})$. The appropriate scaling, using L^*_{com} as the non-dimensional interaction length of the CWsBLI, is

$$L^*_{com} = \frac{L_{com}}{\delta^*_1}\frac{\sin(\varphi_{equ})\sin(\beta)}{\sin(\beta - \varphi_{equ})} = \frac{\dot{m}^*_{out}}{\dot{m}^*_{in}} - 1. \tag{3.12}$$

According to the relationship proposed by Mahalingesh *et al.* (2024), a first-order (linear) polynomial fit was made in the current analysis, which is expressed as

$$L^*_{com}(\xi) = a\, S^*_{com}(\xi) + b, \tag{3.13}$$

where $a = 2.6$ and $b = -1.4$ if the interaction was attached ($S^*_{com} \le 1$), and $a = 12.6$ and $b = -11.5$ if the interaction was separated ($S^*_{com} > 1$). In the definition of equivalent interaction intensity, the parameter m is introduced to adjust the pressure required for the separation of the boundary layer. This parameter is derived by fitting the experimental data presented in figure 10(*a*). Under the constraints imposed by (3.13), solve the optimisation problem of minimising the root mean square error, resulting in $m = 0.65$. It should be noted that the value of m can be influenced by flow conditions such as the Mach number and the Reynolds number. In this study, these parameters are calibrated under specific experimental conditions. Future work should investigate how these parameters vary under different flow conditions in order to enhance the general applicability of the scaling law. For out-of-sample scenarios, when $d \le L_{single}$, $\xi = 1$, and consequently CWsBLI is equivalent to ISWBLI, with $L_{com} = L_{single}$. If $d > L_{single}$, for a given d, then the unknown in (3.13) is only L_{com} and can be found.

Figure 12 illustrates the applicability of the scaling laws when comparing the current CWsBLI data with the SWBLI data from Souverein *et al.* (2013) and Touré & Schülein (2020). It should be noted that the experimental dataset from Souverein *et al.* (2013) and Touré & Schülein (2020) uses different values of k, as indicated by Mahalingesh

https://doi.org/10.1017/jfm.2025.11017 Published online by Cambridge University Press

Type	Mahalingesh *et al.* (2024) method	Current method
SWBLI	$R^2 = 0.99$	$R^2 = 0.99$
CWsBLI	$R^2 = 0.88$	$R^2 = 0.94$

Table 3. Coefficient of determination of first-order polynomial fit $L^* = aS_r^* + b$.

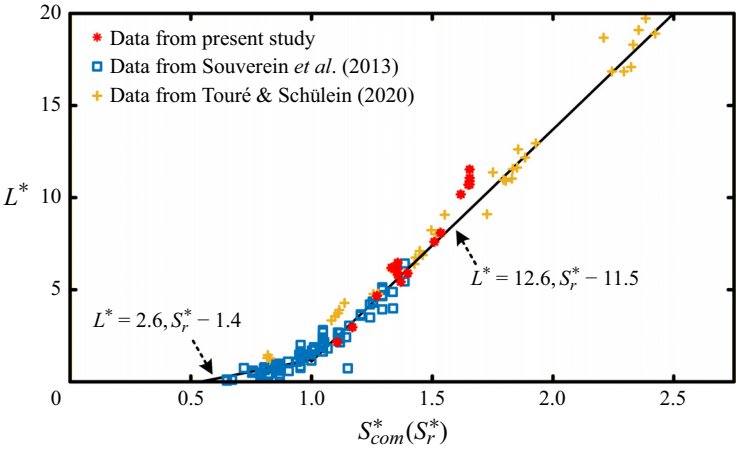


Figure 12. Non-dimensional interaction length and interaction intensity scaling in both SWTBLIs and CWsBLIs.

et al. (2024). Although data from various types of interaction were included, the same normalised method, S_{com}^*, was applied consistently. It was clear that this new scaling law worked in fact for CWsBLI as well. For separated turbulent SWBLIs ($S_r^* > 1$), the interaction intensity exhibits an identical expression form, with a coefficient of determination of 0.99 for both methods, as shown in table 3. Compared with the method proposed by Mahalingesh *et al.* (2024), the approach presented in this study demonstrates a superior fitting performance in separated CWsBLI ($R^2 = 0.94$ versus $R^2 = 0.88$). This improvement is primarily attributed to the incorporation of the effect of the coverage range on the interaction intensity within the model. In the case of SWBLI, the spatial length L_{single} required for the flow to achieve a pressure rise within the SWBLI zone corresponds to the distance required for the loss of momentum to reach zero. As a result, the influence of L_{single} becomes negligible, leading to a simplified expression based solely on the pressure rise or the pressure ratio. In contrast, for CWsBLI, the spatial length required for the pressure rise is affected by the coverage range of the compression waves, resulting in a distinct formulation of interaction intensity. By introducing the concept of equivalent interaction intensity, this study more accurately accounts for the impact of the coverage range of compression waves on the interaction length.

3.4. *Discussion*

As analysed in existing research, the interaction intensity exhibits only a weak dependence on the Reynolds number through the coefficient k. In the case of SWBLIs, the interaction length is directly influenced by the Mach number and the flow deflection angle. In contrast, for CWsBLIs, in addition to these two parameters, the interaction intensity S_{com}^* is also closely related to the spatial extent of the compression waves – or more

https://doi.org/10.1017/jfm.2025.11017 Published online by Cambridge University Press

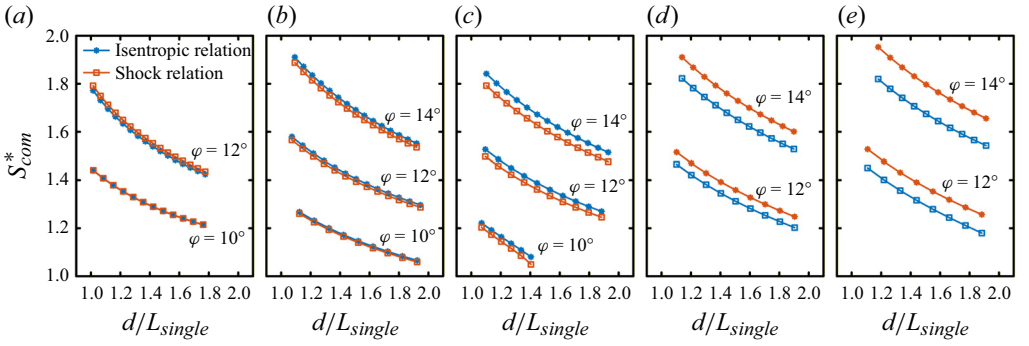


Figure 13. Dependence of S^*_{com} on the Mach number and the flow deflection: (*a*) $M_1 = 2.0$, (*b*) $M_1 = 2.5$, (*c*) $M_1 = 3.0$, (*d*) $M_1 = 3.5$, (*e*) $M_1 = 4.0$. The coverage range d has been normalised based on the interaction length of the ISWBLI under corresponding Mach numbers and flow deflection angles. For the condition $M_1 = 2.0$, a Mach reflection is formed at $\varphi = 14°$; therefore the corresponding results are not included. Similarly, under the conditions $M_1 = 3.5$ and $M_1 = 4.0$ with $\varphi = 10°$, the results are also omitted. The primary reason is that the interaction intensity of the SWBLI under these conditions is relatively low. Even in the presence of SWBLIs, the value of S^*_r generally remains below 1.2.

fundamentally, to the pressure gradient associated with the pressure distribution. This relationship enables the graphical determination of the $M-\varphi-d$ combination, which reveals a distinct tendency of the flow to separate.

Figure 13 illustrates the variation of S^*_{com} with d for different Mach numbers and flow deflection angles. The total pressure ratio in the CWsBLI configuration arises from two distinct components: the flow passing through compression waves and a separation shock. It should be emphasised that the initial pressure ratio employed in the calculation of S^*_{com} is determined based on the assumption of an isentropic process. However, under non-ideal conditions, shock waves may develop during the compression process. To account for this phenomenon, this study adopts an extreme case approach, applying the oblique shock relation to approximate the pressure ratio achieved during compression. The figure also presents a comparison of the evaluation of S^*_{com} based on the isentropic assumption and the oblique shock relation. Furthermore, it should be emphasised that the parameter m in the aforementioned equations is determined based on specific Mach numbers and flow deflection angles. Additional data across a range of operating conditions would be required to validate their broader applicability. Hence the current analysis remains qualitative.

It can be observed that when the Mach number and the flow deflection angle are small, the results obtained using the isentropic assumption and the oblique shock relation are in close agreement. As both the Mach number and the flow deflection angle increase, the discrepancy between the two methods gradually widens. For instance, when $M_1 = 4$, $\varphi = 14°$ and $d/L_{single} \approx 1.6$, the deviation in S^*_{com} becomes 6.8 %. This discrepancy arises primarily from the calculation of the pressure rise. At a constant flow deflection angle, the pressure rise achieved through an isentropic process is greater than that resulting from an oblique shock, especially at higher Mach numbers. Consequently, under the same d/L_{single} and higher Mach numbers, if shock waves occur during the compression process, then employing the isentropic relation for calculations may lead to an overestimation of the actual pressure ratio, as well as the interaction intensity S^*_{com}, thus producing an overestimated interaction length. However, this deviation remains relatively minor at lower Mach numbers, typically in the range Mach 2–2.5.

Although there is a certain deviation between the ideal isentropic process and the actual scenario involving shock waves, the overall trends exhibited by both remain consistent.

https://doi.org/10.1017/jfm.2025.11017 Published online by Cambridge University Press

It can be observed that at a constant flow deflection angle and Mach number, the interaction intensity decreases as the coverage range increases (see (3.8)). For a fixed flow deflection angle and normalised coverage range, an increase in Mach number tends to delay the onset of flow separation, confirming the well-known property. Conversely, an increase in the flow deflection angle promotes flow separation.

The scaling law proposed in this study shows good performance under current experimental conditions; however, additional data obtained under diverse conditions are required to validate its broader applicability.

First, the proposed method exhibits potential advantages in addressing complex SWBLI scenarios, such as dual SWBLIs. For example, previous studies by Li *et al.* (2022, 2023) have indicated that the separation scale in such interactions is significantly influenced by the spacing between the shock waves. By converting dual SWBLIs into equivalent single shock wave configurations, the method offers a simplified yet effective scaling approach for analysing these intricate flow phenomena. Future work should aim to further validate the applicability of this method across a broader range of wave system configurations.

Second, this study employed a curved surface design based on tracing the path of a streamline within the expansion waves passing over a sharp corner. However, the aerodynamic configurations of the actual high-speed inlets may differ due to various factors. For example, considering the constraints of the wall pressure distribution, various aerodynamic profiles can emerge. Therefore, a broader range of curved surface configurations should be taken into account.

In addition, the experiment was conducted at Mach number 2.3 with a turbulent boundary layer. For inlets operating over a wide Mach number range, the upstream flow conditions of the cowl will vary. The interaction characteristics associated with laminar and transitional CWsBLI may differ from those observed in turbulent flows, particularly under conditions involving low Reynolds numbers or high Mach numbers. The applicability of the scaling law under varying Mach numbers, Reynolds numbers, boundary layer conditions and wall conditions requires further validation.

Finally, this study did not account for the influence of three-dimensional effects on flow separation. In practical applications, these factors can significantly affect the dynamics of the boundary layer and the extent of flow separation. Therefore, future research should integrate three-dimensional numerical simulations with experimental investigations to examine how these parameters modify the scaling laws.

4. Conclusion

Scaling laws for SWBLIs are fundamental in predicting flow separation in supersonic and hypersonic flows, but they fail to account for the complexity of CWsBLIs. The spatial coverage range of compression waves introduces unquantified effects on separation, creating a critical gap in the existing literature. This study addresses this gap through the experimental investigation of CWsBLIs induced by curved surfaces, and the development of a unified scaling framework that integrates CWsBLIs with traditional SWBLIs.

Experiments were conducted in the Mach 2.5 supersonic wind tunnel using Z-type schlieren imaging and fast-response pressure transducers, targeting interactions at two flow deflection angles ($\varphi = 10°, 12°$) and varying d. These measurements reveal distinct CWsBLI dynamics that diverge from ISWBLI: unlike the two-step pressure rise and plateau characteristic of ISWBLI, CWsBLIs exhibit sustained pressure increases downstream of the separation point due to continuous interaction between the incident compression waves and the separated shear layer, accompanied by dispersed expansion fans. A critical threshold emerges in the coverage range d relative to L_{single}: when

https://doi.org/10.1017/jfm.2025.11017 Published online by Cambridge University Press

$d \leq L_{single}$, the length scales of the interactions remain comparable to those of the ISWBLIs, though the shear layer and the separation shock angles are reduced; when $d > L_{single}$, the weakened APG drives a progressive reduction in the separation scale, together with a secondary increase in the shock angle due to the decrease in the upstream Mach number. Unsteady measurements further show that the vortex shedding frequencies in the shear layer shift to higher values as d increases, attributed to premature vortex break-up for $d \leq L_{single}$ and shortened shear layer length for $d > L_{single}$.

To resolve the inadequacy of the traditional pressure ratio/pressure rise metrics, an equivalent transformation method grounded in the pressure gradient is proposed. This method converts CWsBLIs into an equivalent ISWBLI with a matched interaction length and intensity, enabling unification with SWBLI scaling. CWsBLIs are classified by L_{single}: for $d \leq L_{single}$, a correction factor $\xi = 1$ applies and the scaling aligns with the existing SWBLI laws; for $d > L_{single}$, $\xi = L_{com}/d$ modifies the equivalent pressure rise and separation pressure ratio, with the equivalent deflection angle φ_{equ} derived through oblique shock relations to compute the geometric factor G_3. This framework achieves superior data collapse: for separated CWsBLIs, the coefficient of determination R^2 increases from 0.88 (Mahalingesh *et al.* 2024) to 0.94, while maintaining $R^2 = 0.99$ for SWBLIs, thereby confirming its capability to effectively unify both types of interactions.

The work advances a fundamental understanding by demonstrating that CWsBLI-induced separation is governed by the coverage range of compression waves. Practically, the derived $M-\varphi-d$ relationship provides a quantitative tool for balancing compression efficiency and flow stability in the design of compression surfaces. However, limitations remain: the framework is validated for turbulent boundary layers at $M_1 \approx 2.3$, and deviations arising from non-isentropic conditions may increase at higher Mach numbers ($M_1 > 3$) in practice. Future work should extend validation to laminar/transitional CWsBLIs, various curved surface configurations, and three-dimensional effects, all of which are critical for accurately representing real inlet geometries.

Acknowledgements. This work was supported by the National Natural Science Foundation of China (grant no. 12002281). The authors would like to express their sincere appreciation to the editor and the referees for their invaluable contributions in enhancing the paper's quality. In addition, special thanks are extended to J. Yang, W. Huang and B. Chang for their valuable assistance in conducting the experiments.

Declaration of interests. The authors report no conflict of interest.

References

Chapman, D.R., Kuehn, D.M. & Larson, H.K. 1957 Investigation of separated flows in supersonic and subsonic streams with emphasis on the effect of transition. *Tech. Rep.* Technical Note 3869. NACA.

Coles, D. 1956 The law of the wake in the turbulent boundary layer. *J. Fluid Mech.* **1**, 191–226.

Fan, X.H., Wang, G., Lin, J.Z., Yang, Y.G. & Tang, Z.G. 2023 Effects of expansion waves on incident shock-wave/boundary-layer interactions in hypersonic flows. *Phys. Fluids* **35** (10), 109901.

Guan, X.K., Bai, C.Y. & Wu, Z.N. 2020 Double solution and influence of secondary waves on transition criteria for shock interference in pre-Mach reflection with two incident shock waves. *J. Fluid Mech.* **887**, A22.

Helm, C.M. & Martin, M.P. 2021 Scaling of hypersonic shock/turbulent boundary layer interactions. *Phys. Rev. Fluids* **6** (7), 074607.

Hong, Y.T., Li, Z.F. & Yang, J.M. 2021 Scaling of interaction lengths for hypersonic shock wave/turbulent boundary layer interactions. *Chin. J. Aeronaut.* **34** (5), 504–509.

Huang, H.X., Sun, S., Tan, H.J., Ning, L. & Wang, J. 2015 Characterization of two typical unthrottled flows in hypersonic inlet/isolator models. *J. Aircraft* **52** (5), 1715–1721.

Jaunet, V., Debieve, J.F. & Dupont, P. 2014 Length scales and time scales of a heated shock-wave/boundary-layer interaction. *AIAA J.* **52** (11), 2524–2532.

Li, N., Chang, J.T., Xu, K.J., Yu, D.R. & Bao, W. 2021 Instability of shock train behaviour with incident shocks. *J. Fluid Mech.* **907**, A40.

https://doi.org/10.1017/jfm.2025.11017 Published online by Cambridge University Press

LI, N., CHANG, J.T., XU, K.J., YU, D.R., BAO, W. & SONG, Y.P. 2018 Oscillation of the shock train in an isolator with incident shocks. *Phys. Fluids* **30** (11), 116102.

LI, N., LI, W.F., YE, Z.Y. & ZHANG, W.W. 2024 On the mean structure and unsteadiness of dual shock wave–turbulent boundary layer interactions. *J. Fluid Mech.* **999**, A3.

LI, X., ZHANG, Y., TAN, H.J., JIN, Y. & LI, C. 2022 Comparative study on single-incident and dual-incident shock wave/turbulent boundary layer interactions with identical total deflection angle. *J. Fluid Mech.* **940**, A7.

LI, X., ZHANG, Y., TAN, H.J., SUN, S., YU, H., JIN, Y. & ZHOU, J. 2023 Separation length scaling for dual-incident shock wave–turbulent boundary layer interactions with different shock wave distances. *J. Fluid Mech.* **960**, A9.

MAHALINGESH, N., PIPONNIAU, S. & DUPONT, P. 2024 A universal scaling for the length scales of shock-induced separation. *J. Fluid Mech.* **1000**, A5.

PANG, M.C., WANG, Z.Y., ZHANG, Y., TAN, H.J., CHEN, L. & ZHANG, H. 2025 Characteristics of incident compression waves/boundary layer interaction for high-speed supersonic inlets. *Phys. Fluids* **37** (1), 016134.

RAMESH, M.D. & TANNEHILL, J.C. 2004 Correlations to predict the streamwise influence regions in supersonic turbulent flows. *J. Aircraft* **41** (2), 274–283.

SECKIN, S., MEARS, L.J., SONG, M., ALVI, F.S. & ZIGUNOV, F. 2023 Surface properties of double-fin generated shock-wave/boundary-layer interactions. *AIAA J.* **61** (12), 5302–5319.

SETTLES, G.S., BOGDONOFF, S.M. & VAS, I.E. 1976 Incipient separation of a supersonic turbulent boundary layer at high Reynolds numbers. *AIAA J.* **14** (1), 50–56.

SOUVEREIN, L.J., BAKKER, P.G. & DUPONT, P. 2013 A scaling analysis for turbulent shock-wave/boundary-layer interactions. *J. Fluid Mech.* **714**, 505–535.

SRIRAM, R. & JAGADEESH, G. 2015 Correlation for length of impinging shock-induced large separation bubble at hypersonic speed. *AIAA J.* **53** (9), 2771–2775.

TOURÉ, P.S.R. & SCHÜLEIN, E. 2020 Scaling for steady and traveling shock wave/turbulent boundary layer interactions. *Exp. Fluids* **61** (7), 156.

TOURÉ, P.S.R. & SCHÜLEIN, E. 2023 Interaction of a moving shock wave with a turbulent boundary layer. *J. Fluid Mech.* **964**, A28.

WANG, C.P., XUE, L.S. & TIAN, X. 2017 Experimental characteristics of oblique shock train upstream propagation. *Chin. J. Aeronaut.* **30** (2), 663–676.

WANG, X., WANG, Z.G., SUN, M.B., WANG, Q.C. & HU, Z.W. 2019 Direct numerical simulation of a supersonic turbulent boundary layer subject to adverse pressure gradient induced by external successive compression waves. *AIP Adv.* **9** (8), 085215.

WANG, Z.G., ZHAO, Y.L., ZHAO, Y.X. & FAN, X.Q. 2015 Prediction of massive separation of unstarted inlet via free-interaction theory. *AIAA J.* **53** (4), 1108–1111.

WEN, J.H., WANG, Q.C., WEI, F., LIN, J.C., ZHOU, Y.M. & LUO, X. 2023 Response of a supersonic turbulent boundary layer to different streamwise adverse pressure gradients. *Phys. Fluids* **35** (9), 095114.

XIE, W.Z., YANG, S.Z., ZENG, C., LIAO, K., DING, R.H., ZHANG, L. & GUO, S.M. 2021 Improvement of the free-interaction theory for shock wave/turbulent boundary layer interactions. *Phys. Fluids* **33** (7), 075104.

ZHANG, H., LI, X., TAN, H.J., SUN, S., WU, J.Y. & ZHANG, Y. 2021 Experimental investigation of dual swept shock wave/boundary layer interactions. *J. Vis.* **24** (6), 1115–1122.

ZUO, F.Y. 2023 Hypersonic shock wave/turbulent boundary layer interaction over a compression ramp. *AIAA J.* **61** (4), 1579–1595.

https://doi.org/10.1017/jfm.2025.11017 Published online by Cambridge University Press